Non-destructive monitoring of internal temperature distribution in prismatic Li-ion battery cells with ultrasonic travel-time tomography

Abstract

Large prismatic Li-ion battery cells are increasingly becoming the primary power source for transportation applications. Online thermal management of these cells is crucial for ensuring safety and maximizing performance. However, due to the prismatic design, significant discrepancies arise between surface and internal temperatures, making it difficult to detect internal thermal anomalies in time to prevent irreversible thermal hazards. This paper introduces a ground-breaking technology for the thermal management of prismatic batteries, offering non-destructive, real-time imaging of internal thermal anomalies. It leverages the sensitivity of ultrasound speed to temperature, combined with tomographic reconstruction based on surrounding measurements, to provide detailed cross-sectional thermal imaging. The system is compact, economical, and suitable for in-situ deployment, serving as a precise feedback mechanism for online thermal management. Demonstrated in continuous discharging scenarios, the technology reveals a high-temperature region near the tabs, which is undetectable by surface-mounted thermocouples. This advancement holds potential to significantly reduce the risk of fires and explosions in electric vehicles.

Keywords: Battery management, Electric vehicles, Li-ion batteries, Thermal runaway, Ultrasound tomography

Introduction

Large prismatic Li-ion battery cells are indispensable power sources in transportation applications. However, they are particularly vulnerable to thermal runaway under abusive conditions [1]. Scenarios such as fast charging/discharging [2], internal short-circuit, and external heating typically cause a significant rise in battery temperature. When the temperature reaches a critical range, it can trigger irreversible thermal runaway [3, 4], potentially leading to fires and explosions. Given the severity of these hazards, it is crucial to prevent the temperature from exceeding safe thresholds. Elevated temperatures also accelerate the formation and repair of the solid electrolyte interface (SEI) layer, which can deplete active lithium during cycling and result in rapid capacity loss [5, 6].

In addition to high-temperature risks, low temperatures can reduce electrolyte conductivity and slow down the diffusion of lithium ions, leading to voltage drops and capacity loss [7]. Operating batteries in cold environments can also cause lithium plating [6], which increases the risk of internal short-circuit [8], electrolyte decomposition [9], and potentially thermal runaway [10].

In summary, maintaining an optimal operating temperature throughout the battery's life cycle is essential for preventing both lithium plating and thermal runaway, while also maximizing performance and longevity [11]. Consequently, in-situ and real-time monitoring of battery temperature during operation is vital.

Surface temperature measurements are relatively straightforward using thermocouples and thermal imaging systems. However, the large prismatic design of batteries creates substantial differences between internal and surface temperatures. Self-heating during operation can significantly elevate the internal temperature of Li-ion batteries while heat transfer from the interior to the exterior is impeded by the battery's multi-layered structure and the low thermal conductivity of its components [12]. This results in considerable temperature gradients across the battery's thickness. In a 280 Ah prismatic cell, the temperature difference across the thickness can reach up to 26.2 °C [13]. Additionally, during fast charging or discharging, the current concentration near the tabs can lead to non-uniform temperature distribution within the plane of layers [14–20]. These thermal inhomogeneities can exacerbate inhomogeneous degradation, which significantly compromises the safety of Li-ion batteries [21, 22]. Furthermore, internal short-circuit can create localized high-temperature regions [23–25], which may quickly escalate to thermal runaway. It is therefore essential to have an in-situ and real-time internal temperature mapping technique that ensures optimal conditions throughout the cell.

However, despite extensive efforts over the years, effective internal temperature monitoring remains a challenge in the rapidly growing electric vehicle market. In practice, thermocouples are often attached to the negative or positive poles to estimate the highest internal temperature under normal operating conditions. However, this method does not provide a true representation of internal temperature [15, 17, 18] and is ineffective under abnormal conditions. A recent study [26] employed X-ray diffraction for internal temperature measurement, but this method is unsuitable for in-situ monitoring. Existing in-situ internal temperature monitoring technologies can be broadly categorized into three main approaches: embedded thermal sensors, model-based estimation, and impedance-based estimation [12]. Temperature sensors, such as resistance temperature detectors (RTDs) [27], thermocouples [13, 14, 28], and fiber Bragg grating (FBG) sensors [29], are embedded within Li-ion batteries to measure temperature directly. However, these sensors inevitably degrade battery performance.

Alternatively, model-based methods have been developed to predict internal temperature using measurable parameters like current and voltage, but these models often struggle to balance accuracy and efficiency in complex scenarios [22]. Another non-destructive approach involves estimating internal temperature based on electrochemical impedance, a temperature-dependent parameter. However, this method only provides an average temperature [22], whereas, in real applications, the temperature distribution is typically uneven, with significant differences between the maximum/minimum and the average temperatures.

The lack of effective monitoring technologies continues to be a significant barrier to the thermal safety of electric vehicles, underscoring the urgent need for an in-situ and real-time internal temperature mapping technology [30]. Non-destructive testing using penetrative ultrasonic waves has emerged as a promising tool for estimating the internal state of batteries [31, 32]. In addition to being non-destructive, ultrasonic testing is low-power, efficient, compact, affordable, and standalone, making it well-suited for in-situ and real-time monitoring tasks.

Recent studies have demonstrated the sensitivity of ultrasonic features to internal temperatures [33, 34], suggesting that ultrasound can be used to diagnose internal temperature. Although a quantitative explanation of the temperature effect on ultrasound remains underexplored, it is generally attributed to the temperature-dependent mechanical properties of battery components.

To map temperature distribution and detect abnormal thermal events at any location, ultrasonic tomography, which has proven valuable in applications such as breast cancer screening [35, 36], emerges as a strong candidate. This technique provides fast, non-destructive cross-sectional imaging by projecting ultrasonic waves from various angles in a two-dimensional space. As these waves traverse an object, their features, such as amplitude and travel time, change in response to the object's internal properties along the wave's path. Tomographic reconstruction is then employed to compute the distribution of acoustic properties within the imaging region, such as sound speed and acoustic attenuation. Since acoustic properties correlate directly with temperature, the temperature distribution can be inferred from the acoustic property distribution [37, 38].

The objective of this paper is to devise a customized ultrasonic tomography system for monitoring internal temperatures in prismatic cells. This system is designed to be low-power, compact, cost-effective, non-destructive, and highly efficient, facilitating in-situ and real-time internal temperature monitoring for each cell in electric vehicles, as illustrated in Fig. 1. This technology would serve as a groundbreaking feedback mechanism for thermal management systems, ensuring optimal working conditions and reducing the risk of thermal runaway in batteries. It represents a significant breakthrough in enhancing the safety of electric vehicles.

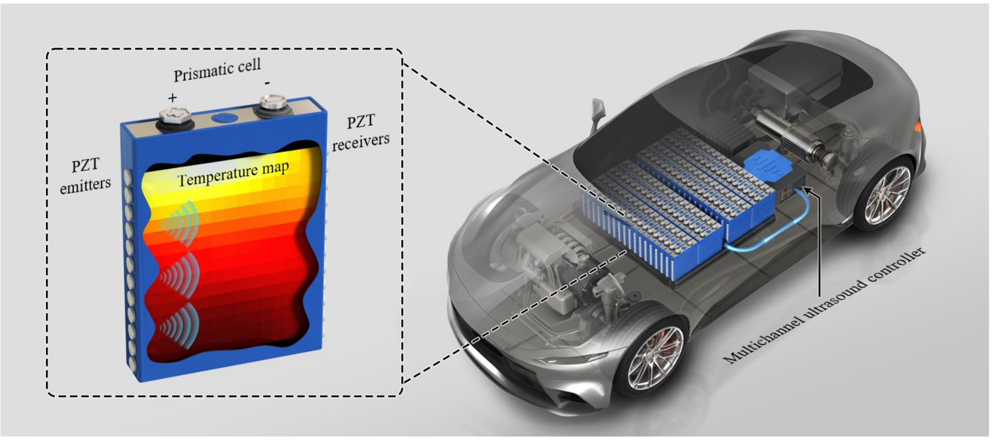

Fig. 1 Schematic of in-situ monitoring of the internal temperature distribution within each cell of an electric vehicle using an ultrasonic tomography system.

Results

Configuration of the imaging system

The prismatic cell used for demonstration is a commercial $LiFePO_4$ prismatic cell with a rated capacity of 50Ah (EVE LF50K). As visualized by the X-ray CT in Fig. 2a, the prismatic cell contains two rolls of prismatically winded electrode/separator layers.

Ultrasonic tomography enables cross-sectional imaging using ultrasonic transducers arranged around the cross-section. These transducers emit unfocused cylindrical ultrasonic waves and receive the transmitted waves, ensuring full coverage of the cross-section.

The imaging cross-section is in the plane of the mid-layers of an electrode roll. This plane was selected for several reasons: 1) Thermal abnormalities typically occur internally, with thermal conduction in the out-of-plane direction being much smaller than in the in-plane direction [39]. Thus, thermal abnormalities can be detected in the mid-layers earlier than in any cross-sections parallel to the bottom or side views. 2) The mid-layer plane is mostly homogeneous, simplifying wave propagation. Conversely, if the imaging plane is parallel to the side or bottom views, with ultrasonic transducers on the front and back surfaces, the wave propagation path becomes highly inhomogeneous, causing strong refraction due to the inclined transmission of the layers. 3) Electrolyte gaps at the side corners necessitate placing ultrasonic transducers on the mid-layer plane, where the gap thickness is minimal, to promote transmission through the gap.

Given the rectangular cross-section, ultrasonic transducers should be arranged in four linear arrays, each placed on one side of the cross-section to achieve a complete range of projection angles for tomography. However, the presence of the electrolyte/air region at the top of the cell and the electrolyte gaps at the corners and bottom hampers effective ultrasonic wave transmission. High-quality signals can only be obtained from the left and right sides of the mid-layer plane. Consequently, only two arrays of ultrasonic transducers are used, with one set of transducers acting as emitters on one side of the battery and another set acting as receivers on the opposing side, creating a parallel setup. This configuration results in a typical limited-angle tomography problem.

As illustrated in Fig. 2b, the plane of imaging is not fully homogeneous. At both the left and right sides, the electrode/separator layers are rolled. As a result, the layers are perpendicular to the imaging plane at these sides, leading to a through-thickness or an inclined wave transmission of the layers. For a wave propagation from an emitter to the opposite receiver, the excited waves first propagate through the thickness direction of the side layers and then along the mid-layers. We may simplify wave propagation as part through-thickness transmission and part in-plane transmission. For the inclined transmission in the inhomogeneous region of the imaging plane, the wavefront can be elliptical due to the anisotropy of the stacked layers at the macro scale. This implies the wave propagation path within this area is curved. However, considering the small curvature, the limited size of the inhomogeneous region, and the low resolution required for temperature mapping, we simplify the path within this area as a direct line.

Given the mixing of through-thickness and in-plane transmission within one path, additional measurements are needed to determine their temperature effects separately. Thus, supplementary ultrasonic transducers are placed on the front and back surfaces for through-thickness transmission measurements, as shown in Fig. 2a. These transducers can also provide through-thickness-averaged temperatures at their locations after temperature effect calibration, serving as cross-validation for the tomography results.

The ultrasonic emitters and receivers are PZT disks, which can convert energy between vibrations and voltages. As depicted in Fig. 2c, the applied or reacted electric field is parallel to the polarization direction. Consequently, both in-surface and out-of-surface displacements can be generated and sensed. However, the in-surface displacements excite strong S_0 mode Lamb waves propagating in the prismatic shell. Although the shell corners and internal leakage dampen the Lamb waves, their presence is still significant. To suppress Lamb wave interference and receive pure bulk longitudinal waves propagating internally, soft adhesives that only maintain out-of-surface displacement continuity are used to bond the PZT disks to the surface.

Fig. 2d shows example denoised signals excited by the top emitter at 25 °C and a fully charged state. Each received signal contains a distinct bulk wave packet with a center frequency of 0.2 MHz. Based on the arrival times of the ultrasonic waves, indicated by the red dots in Fig. 2d, the wave velocity is approximately 2400 m/s. Consequently, the wavelength is approximately 12 mm.

The height of the imaging area is limited by the emitter's beam angle range, which is approximately $\pm 45°$. As shown in Fig. 2e, the height is 144 mm, slightly smaller than the height of the electrode rolls. The center-to-center distance between two neighboring emitters/receivers is 12.7mm, given their diameter of 10mm. Consequently, there are 12 emitters/receivers. The emitters sequentially excite waves at approximately 5 ms intervals, ensuring the waves from the previous emitter fully dissipate and allowing each receiver to record waves from each emitter individually. This step results in 12×12 emitter-receiver signal channels, with the propagation paths covering the entire imaging area.

Given that the imaging plane is nearly homogeneous, and the temperature distribution is continuous with small gradients, the diffraction and refraction of ultrasonic waves can be neglected. This allows the propagation of ultrasonic waves from the emitter to the receiver to be approximated as straight rays. Under this approximation, travel times are treated as line integrals of local slowness (inverse of velocity) along ray paths [37, 38, 40, 41]. A slowness map can be reconstructed using a tomography

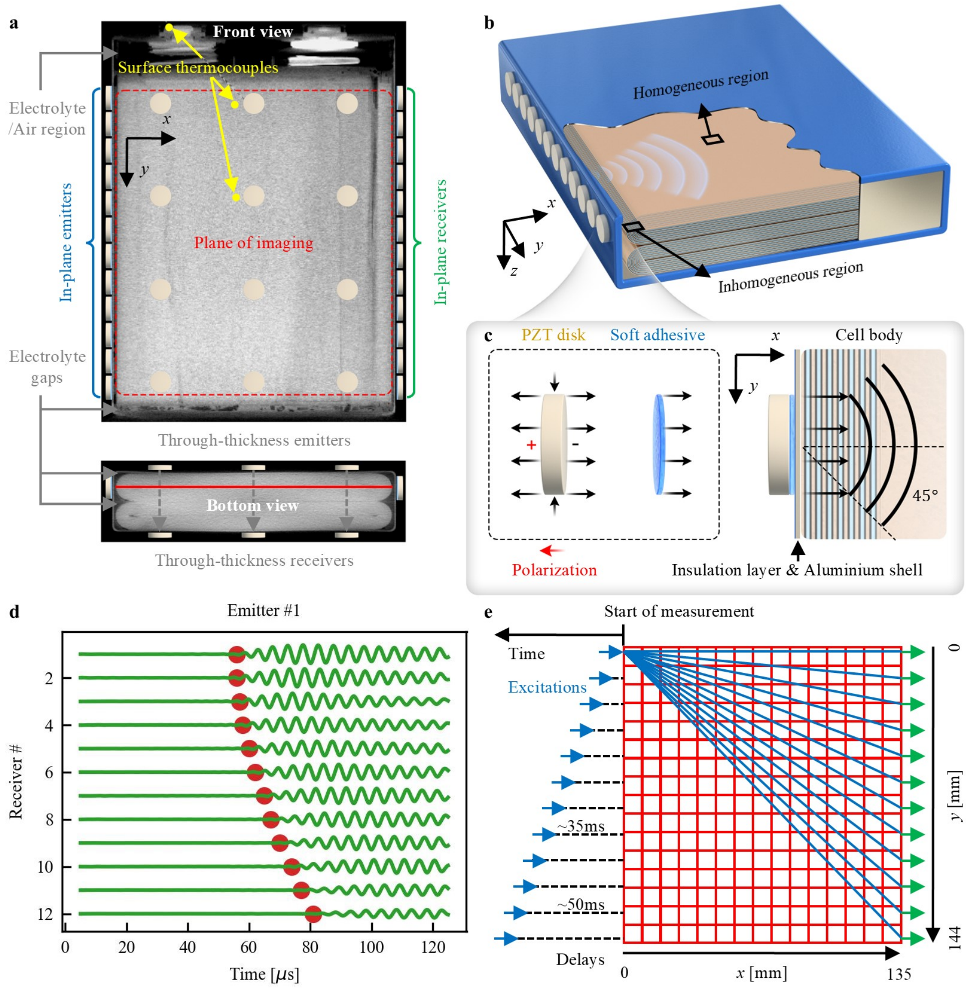

Fig. 2 Configuration of ultrasonic travel-time tomography for imaging internal temperatures in a prismatic Li-ion battery cell. a The internal structure of the prismatic cell revealed by X-ray CT, showing two rolls of prismatically winded electrode/separator layers and electrolyte/air gaps in a rigid shell. This panel also includes a schematic of the imaging plane and the placement of ultrasonic emitters/receivers. **b** Schematic of wave propagation in the imaging plane, which contains two inhomogeneous regions at the sides and a main homogeneous region. In the inhomogeneous regions, the propagation direction is right/inclined through the thickness of the layers, while in the homogeneous region, it is along the plane of layers (in-plane transmission). **c** Soft adhesive to selectively generate and receive out-of-surface displacements. **d** Example denoised signals excited by the top emitter with red dots indicating arrival times based on a speed of 2400 m/s. **e** Illustration of the sequential excitation order of ultrasonic waves (5ms interval to avoid interference), wave propagation paths, and discretization of the imaging area. The data collection time is less than 0.1s.

process adapted from the approach used in X-ray CT-based reconstruction systems [36].

Since this is a typical limited-angle and sparse-view tomography problem, a direct solution is not feasible, necessitating the discretization of the imaging area for a numerical solution [42]. The pixel size is set to 9 mm, resulting in a grid of 16 × 15 pixels.

With the ultrasonic waves approximated as straight rays and the imaging area discretized, the travel times can be expressed with a linear system:

$$\mathbf{t} = W\mathbf{s}, \tag{1}$$

where $\mathbf{t} \in \mathbb{R}^{144\times 1}$ includes the arrival times of 144 emitter-receiver channels, $\mathbf{s} \in \mathbb{R}^{240\times 1}$ includes the slowness (inverse of velocities) of all pixels, and the element $W[i, j]$ in $W \in \mathbb{R}^{144\times 240}$ represents the intersection length between the i-th emitter-receiver path and the j-th pixel.

In practice, due to the noisy and weak signals, extracting accurate travel times is challenging. Instead, we use signals at 25°C and the fully charged state as baselines and calculate the shifts in travel times $\Delta\mathbf{t}$ between the current signals and the baselines by comparing their full waveforms. The extraction of $\Delta\mathbf{t}$ is more accurate and robust than that of $\mathbf{t}$ due to the consideration of the full waveform. As a result, Eq. 1 becomes

$$\Delta\mathbf{t} = W\Delta\mathbf{s}. \tag{2}$$

Tomographic reconstruction involves solving this linear system using Algorithm 1 (described in Methods) with the measured arrival times as input. Once the slowness distribution is determined, the temperature distribution can be derived using the correlation between slowness and temperature obtained through temperature effect calibration.

Temperature effect calibration

The cell equipped with the ultrasonic system was placed in a climatic chamber. To calibrate the temperature effect on ultrasonic slowness, the climatic chamber maintained a specific temperature for several hours to create a uniform temperature distribution within the battery. As a result, the shifts of travel times, $\mathbf{\Delta t}$, due to the transition from the baseline temperature (25°C) to the current temperature can be obtained. By varying the temperature in the chamber and repeating this process, the temperature effect on slowness can be obtained.

Fig. 3a presents the in-plane travel times, $\mathbf{\Delta t}_{xy}$, measured across 144 emitter-receiver channels at four different temperatures, demonstrating a clear linear correlation. The temperature effect of the in-plane travel times, $(\mathrm{d}\mathbf{t}/\mathrm{d}T)_{xy}$, is subsequently determined through linear regression on this data, as shown in Fig. 3b. Similarly, the temperature effect of the through-thickness travel time, $(\mathrm{d}t/\mathrm{dT})_{zz}$, is obtained by taking the average of the results from 12 through-thickness channels, as illustrated in Fig. 3c.

The horizontal propagation from an in-plane emitter to its opposite receiver is equivalent to the sum of through-thickness transmission in the two inhomogeneous regions and in-plane transmission in the homogeneous region. The temperature effect of travel time at the inhomogeneous regions should be half of $(\mathrm{d}t/\mathrm{dT})_{zz}$, as the total width of the inhomogeneous regions is half of the cell thickness. Thus, the temperature effect of the slowness at the homogeneous region can be expressed as:

$$\begin{aligned}(\mathrm{d}s/\mathrm{d}T)_{\mathrm{homogeneous}} &= \frac{(\mathrm{d}t/\mathrm{d}T)_{\mathrm{homogeneous}}}{w_{\mathrm{homogeneous}}} \\ &= \frac{[(\mathrm{d}t/\mathrm{d}T)_{xx} - (\mathrm{d}t/\mathrm{d}T)_{zz}/2]}{w_{\mathrm{homogeneous}}},\end{aligned} \quad (3)$$

where $(\mathrm{d}t/\mathrm{dT})_{xx}$ represents the average of temperature effects for the 12 horizontal (x-direction) propagation channels and $w_{\text{homogeneous}}$ is the width of the homogeneous region.

As $(\mathrm{d}s/\mathrm{d}T)_{\text{homogeneous}}$ is identical at different directions within the imaging plane, we can use it to derive the temperature effects in the inhomogeneous regions for any transmission directions, $(\mathrm{d}\mathbf{s}/\mathrm{d}T)_{\text{inhomogeneous}} \in \mathbb{R}^{144\times 1}$, as follows:

$$(\mathrm{d}\mathbf{s}/\mathrm{d}T)_{\text{inhomogeneous}} = \frac{(\mathrm{d}\mathbf{t}/\mathrm{d}T)_{xy} - (\mathrm{d}s/\mathrm{d}T)_{\text{homogeneous}}\,\mathbf{l}_{\text{homogeneous}}}{\mathbf{l}_{\text{inhomogeneous}}}, \quad (4)$$

where $\mathbf{l}_{\text{homogeneous}} \in \mathbb{R}^{144\times 1}$ and $\mathbf{l}_{\text{inhomogeneous}} \in \mathbb{R}^{144\times 1}$ include the propagation lengths of 144 emitter-receiver channels in the homogeneous region and the inhomogeneous regions, respectively.

The results are visualized in Fig. 3d. The angle represents the propagation angle with the x-axis (horizontal). We can observe that, the temperature effect in the inhomogeneous region is several times larger than that in the homogeneous region. Additionally, this difference diminishes as the angle approaches 90°, which is equivalent to homogeneous propagation.

The significant difference between homogeneous and inhomogeneous temperature effects can create spatial discontinuities in $\Delta\mathbf{s}$, which is not ideal for the tomographic reconstruction algorithm. To ensure the continuity of $\Delta\mathbf{s}$, scaling factors $\alpha = \frac{(\mathrm{d}\mathbf{s}/\mathrm{d}T)_{\text{inhomogeneous}}}{(\mathrm{d}s/\mathrm{d}T)_{\text{homogeneous}}}$ are applied to the elements in W corresponding to pixels intercepting with the inhomogeneous regions.

The temperature effect is primarily attributed to the temperature dependence of material properties, including the stiffness of solids, the sound speed of fluid, and the thermal expansion.

The thermal expansion is typically very small, with a relative size change on the order of 10^{-5} per unit change in temperature, which can be neglected. The change

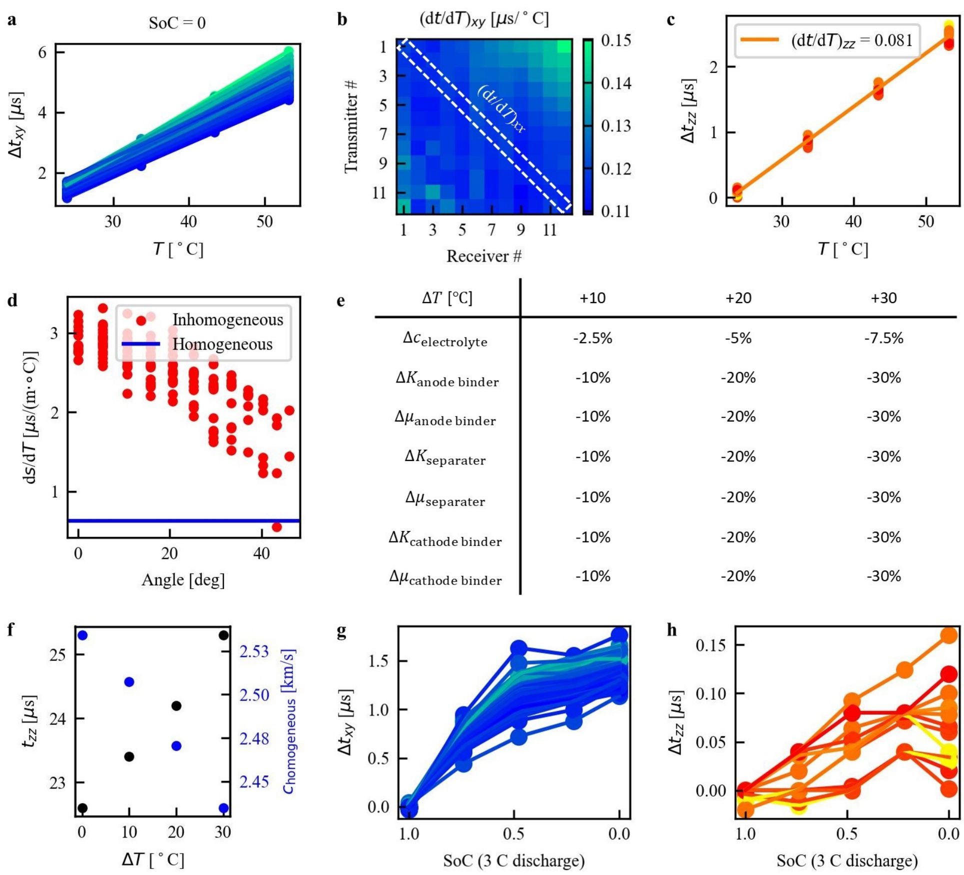

ΔT [°C]	+10	+20	+30
$\Delta c_{\mathrm{electrolyte}}$	-2.5%	-5%	-7.5%
$\Delta K_{\mathrm{anode\ binder}}$	-10%	-20%	-30%
$\Delta \mu_{\mathrm{anode\ binder}}$	-10%	-20%	-30%
$\Delta K_{\mathrm{separater}}$	-10%	-20%	-30%
$\Delta \mu_{\mathrm{separater}}$	-10%	-20%	-30%
$\Delta K_{\mathrm{cathode\ binder}}$	-10%	-20%	-30%
$\Delta \mu_{\mathrm{cathode\ binder}}$	-10%	-20%	-30%

Fig. 3 Temperature effect calibration, simulation, and SoC effect. a Evolution of travel time of each in-plane channel t_{xy} with temperature. **b** Temperature effect $(\mathrm{d}t/\mathrm{dT})_{xy}$ of the in-plane channels obtained by linear fitting. The diagonal values correspond to the temperature effect for horizontal transmissions, $(\mathrm{d}t/\mathrm{dT})_{xx}$. **c** Evolution of travel time of each through-thickness channel t_{zz} with temperature and the temperature effect $(\mathrm{d}t/\mathrm{dT})_{zz}$ obtained by linear fitting and channel-wise averaging. **d** Temperature effect of the slowness of each in-plane channel in the inhomogeneous regions, $(\mathrm{d}s/\mathrm{d}T)_{\mathrm{inhomogeneous}}$, and the temperature effect in the homogeneous region, $(\mathrm{d}s/\mathrm{d}T)_{\mathrm{homogeneous}}$. The horizontal axis represents the propagation angle relative to the x-direction for in-plane channels. **e** The temperature-dependent input parameters for temperature effect simulation. **f** Temperature effects by simulation. **g** The SoC effect on travel time during a 3 C discharge for in-plane channels and **(h)** through-thickness channels.

in stiffness of crystalline materials (Al, Cu, Graphite, and $LiFePO_4$) is also small, typically on the order of 10^{-4} in relative change [43, 44].

In contrast, the stiffness of plastics (binders and separators) is more sensitive to temperature, with changes on the order of 10^{-2} [45, 46]. Moreover, the relative change in sound speed in electrolytes is about 2.5×10^{-3} [47].

A quasi-1-D through-thickness wave propagation model was used to evaluate the effects of these parameter changes, as listed in Fig. 3e, on the through-thickness travel time. The results, listed in Fig. 3f, show that the simulated travel time has a linear correlation with temperature, with a coefficient of 0.089 μs/°C, which is close to the experimental value shown in Fig. 3c.

Additionally, a quasi-1-D numerical model for in-plane wave propagation along the layers was established. The computed velocities range from 2534 m/s to 2435 m/s with the temperature-dependent input parameters, as shown in Fig. 3f. Consequently, we have a simulated $(\mathrm{d}s/\mathrm{d}T)_{\mathrm{homogeneous}}$ of 0.542 μs/(m·°C), which is close to the experimental value in Fig.3d.

SoC effect compensation

In addition to temperature effects, the travel time of ultrasonic waves within the imaging plane is also sensitive to the state of charge (SoC). Therefore, it is crucial to decouple the influences of SoC and temperature before proceeding with temperature imaging. Fortunately, these effects are independent of each other, as the temperature-dependent parameters identified through simulation are uncorrelated with SoC. Consequently, the SoC effect can be compensated first. Notably, since temperature and SoC effects are independent, compensating for SoC at a single temperature is sufficient.

SoC compensation is achieved through partial charge/discharge experiments. After each quarter-cycle of charging or discharging, a resting phase allows the battery to stabilize thermally and return to room temperature (25°C). The travel time corresponding to the current SoC is then recorded. By repeating this process, a relationship between SoC and travel time during 3 C discharge is established, as shown in Fig. 3g and h. The results indicate that while through-thickness travel time is relatively insensitive to SoC, in-plane travel time shows significant sensitivity to SoC. Using this correlation and the SoC provided by coulombic counting, the travel time during a full discharge at 3 C can be compensated for SoC effects.

Another consideration is the potential for local SoC distribution variations at the same overall SoC due to SoC inhomogeneity [48]. To avoid this source of error, the discharges and charges are repeated under the same conditions to ensure that the SoC distribution after partial discharge or charge matches that during the full discharge or charge process being imaged.

Temperature monitoring under an external heat source

In practice, active thermal management with external heating or cooling sources is applied to keep batteries within an optimal thermal range. Additionally, unexpected external heat sources can potentially trigger thermal runaway, making it crucial to evaluate the thermal performance of batteries subjected to external heat.

In this study, a small heat plate was attached to the bottom surface at the bottom right corner of the battery. The temperature evolution with continuous heating at 50 °C is shown in Fig. 4. The internal temperature gradually increased from the bottom right corner, reaching a maximum of 31.6 °C after 27 minutes, which is 4.2 °C higher than the ambient temperature. The overall efficiency of heat conduction was not particularly high.

To validate the temperatures provided by the tomography algorithm, the thickness-averaged temperatures obtained through the temperature effect calibration of the through-thickness travel times at 12 positions (as depicted in Fig. 2a) are used as a reference. The internal temperatures over time at these 12 positions are plotted in Fig. 5, alongside the thickness-averaged temperatures. Although the averaged temperatures

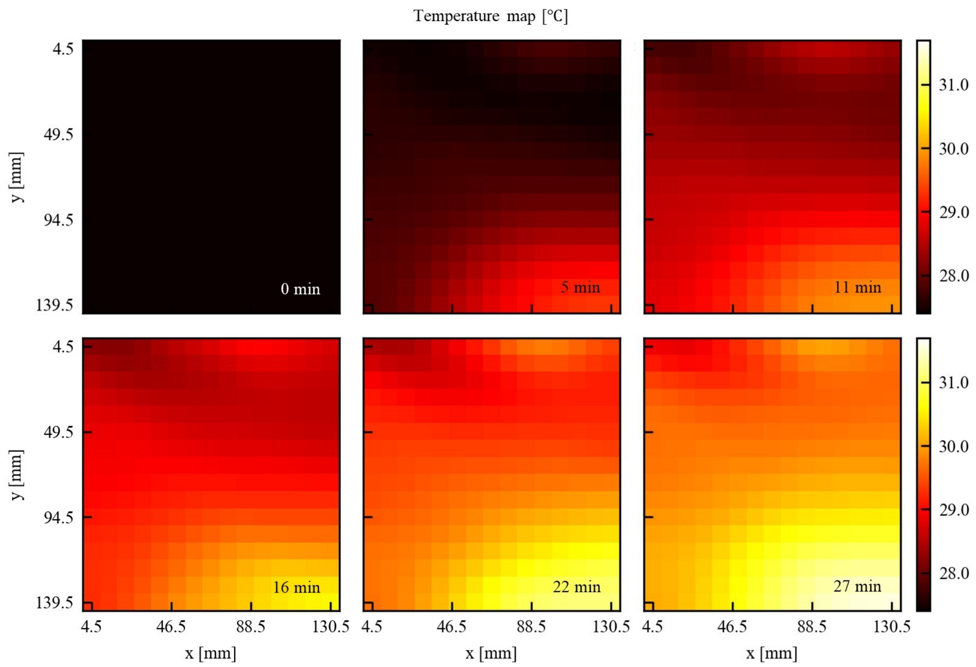

Fig. 4 The internal temperature distributions subjected to a 50 °C external heat source located at the bottom right corner. The video showcasing the experimental setup and real-time temperature mapping is included in the supplementary material.

show some rounding errors due to the ultrasonic signal sampling frequency, the internal and average temperatures are close at most positions, indicating that the tomography algorithm is well validated.

At positions farther from the heat source, the internal temperature tends to be higher than the average temperature. This is reasonable because heat convection at the surface dominates at these locations, leading to a thermal gradient in the thickness direction.

Temperature monitoring during the continuous discharging

In practice, the most demanding conditions for a cell occur during full charges or discharges at high rates. Given that the maximum charge/discharge rate of the prismatic

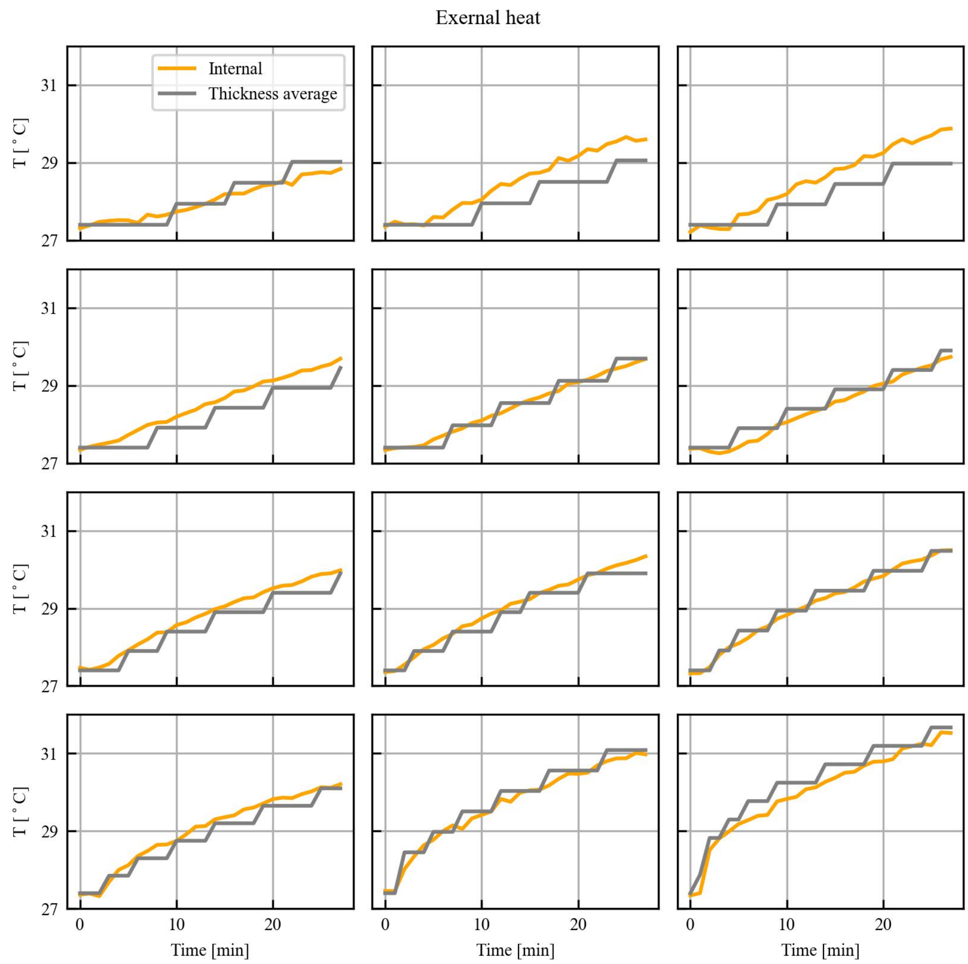

Fig. 5 Local temperature evolution over time at the 12 through-thickness measurement positions depicted in Fig. 2a, subjected to a 50 °C external heat source located at the bottom right corner. Each subfigure plots the temperature at a single position, with the subfigures arranged to correspond to their actual relative positions.

cell is 3 C and the highest operating temperature is 55 °C, the cell's thermal performance was evaluated during a full discharge at 3 C, with an ambient temperature maintained at 25 °C by a chamber.

Each minute, the SoC-compensated travel time shifts were processed using Algorithm 1, and the resulting slowness map was converted into a temperature map based on the temperature effect calibration.

Figure 6 displays snapshots of the internal temperature distribution during a full discharge at a 3 C rate. A vertical thermal gradient emerges early in the discharge, with a higher temperature region consistently near the positive pole. By the end of the discharge, the maximum temperature reaches 46.3 °C, which is 22.5 °C above ambient temperature. At any given moment, the temperature difference can be as much as 8 °C, underscoring the importance of temperature mapping. This thermal inhomogeneity is attributed to current concentration and heat generation near the poles.

The internal temperatures at the 12 through-thickness measurement positions were extracted for further analysis in the time domain and compared with temperatures measured by other tools. As shown in Fig. 7, during the fast discharge, the temperature increase rate exhibited three distinct stages: fast, slow, and then fast again, consistent with simulations and experiments reported in the literature [13–15, 17, 20, 27]. During the subsequent resting stage, the overall temperature gradually decreases, and the thermal inhomogeneity diminishes.

The average temperature across the thickness, as measured by the through-thickness transducers, follows the same trend as the internal temperature at one-quarter thickness. However, the average temperature is consistently lower than the internal temperature, particularly in the top region. This similarity in the evolution pattern validates the internal temperature reconstruction obtained through tomography. Meanwhile, the observed bias between internal and average values confirms the presence of temperature inhomogeneity along the thickness direction.

Surface temperatures measured by two type-K thermocouples at the positions shown in Fig. 2a also follow a similar pattern to the internal and average temperatures at the those positions. However, these surface temperatures are consistently the

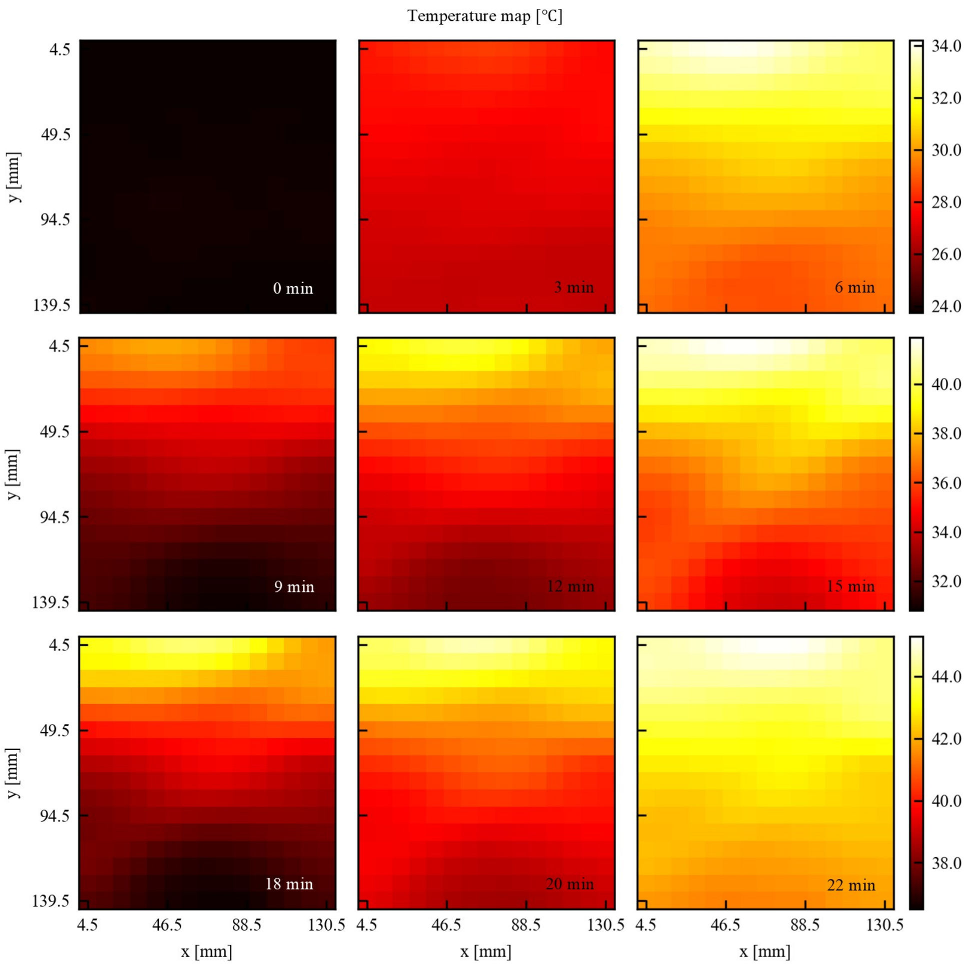

Fig. 6 The internal temperature distributions during a full discharge at 3 C.

lowest, which is expected. The maximum difference between internal and surface temperatures can be as much as 5.9 °C. In contrast, the temperature at the positive pole is significantly higher than the other measured temperatures, reaching up to 73 °C. This observation aligns with the findings of previous experiments [15, 17, 18], indicating substantial heat generation at the battery poles and tabs, contributing to the high-temperature regions near these components.

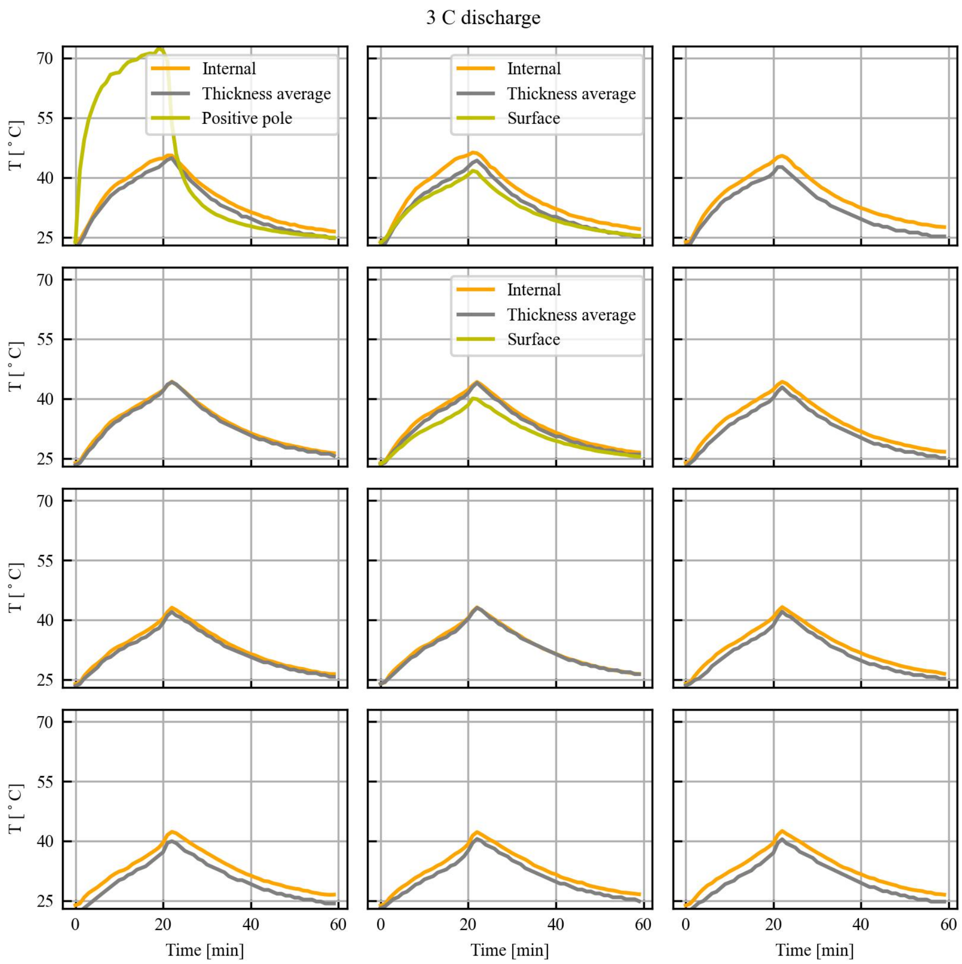

Fig. 7 Local temperature evolution over time at the 12 through-thickness measurement positions depicted in Fig. 2a during a full discharge at 3 C and the subsequent resting stage. Each subfigure plots the temperature at a single position, with the subfigures arranged to correspond to their actual relative positions.

Discussion

This paper presents a groundbreaking technology enabling non-destructive, in-situ, and real-time imaging of internal temperatures within a prismatic cell. This was achieved through the development of an ultrasonic tomography imaging system, which addresses the limited-angle challenge for tomographic reconstruction using smoothing regularization (described in Methods). The technology has been systematically validated using synthetic data (shown in Fig. 8), surface thermocouples, and thickness-average measurements.

Through case studies involving external heating and fast discharging, the internal temperature distribution under realistic operational conditions was imaged for the first time. The external heating case reveals that the heat conduction efficiency is limited in prismatic cells, emphasizing the need for internal temperature monitoring to maintain the thermal state within an optimal range and detect anomalies early. During full and fast discharge, the thermal gradients of up to 8 °C were observed within the imaging plane and 5.9 °C in the cell-thickness direction, underscoring the importance of internal temperature mapping.

For larger and thicker prismatic cells, the overall heat conductivity may be lower, leading to even higher internal temperatures and greater thermal gradients. As an example, the supplementary material includes the temperature evolution of a larger but otherwise identical prismatic cell with a rated capacity of 105 Ah. During a 0.5 C discharge, the maximum temperature approaches that of the 50 Ah cell at a 2 C discharge rate.

Thanks to its compact, low-power, and cost-effective design, this ultrasonic imaging system can act as a real-time feedback mechanism for online thermal management in electric vehicle battery packs. By continuously monitoring internal temperatures, it helps maintain an optimal thermal range, minimizing risks of thermal runaway and lithium plating under regular operating conditions. The system is also crucial for early detection of internal thermal anomalies during abnormal events, such as internal short-circuit or mechanical abuse, enabling prompt intervention to prevent further damage — an invaluable capability for the rapidly growing electric transportation market. Supplementary material includes an example of an abnormal 2 C discharge scenario, where poor contact at the negative pole leads to an internal temperature 7 °C higher than in a typical 2 C discharge.

Moreover, this technology has valuable applications as an offline testing tool for verifying battery thermal properties and designs, as well as for quality control of new cells, contributing to safer, more reliable batteries.

Currently, the system is limited to monitoring temperatures at one-quarter thickness due to the internal structure of the cell. This limitation can be addressed by modifying the cell structure to use stacked electrode layers or by improving the efficiency of ultrasonic transducers. The industry trend toward stacked electrode layers in prismatic cells, rather than rolled layers, reduces corner gap areas, enhancing the effectiveness of this technology.

In the future, errors arising from temperature effect calibration, SoC effect compensation, and the limited range of projection angles should be quantified using additional measurement tools, such as embedded thermal sensors.

Methods

Experiments

PZT-5 disks with dimensions of Φ10 mm $\times$ 2 mm are used as ultrasonic emitters and receivers. These disks are polarized in the thickness direction (2 mm), with the positive electrode coated on the top surface and the negative electrode on the bottom surface. Upon application of a voltage, the disks exhibit both radial and out-of-plane displacements. The natural frequency of the disks is 200 kHz. The bottom surface of each disk is bonded to the cell surface to facilitate wave transmission. For ease of wiring, the negative electrode is equipped with an extra tab that extends to the top surface. The adhesive used for bonding is the 3M 468MP double-sided adhesive with a thickness of 0.13 mm.

The MicroPulse LTPA from Peak NDT[1] was used for generating and receiving electronic signals. A negative pulse with an amplitude of 70 V and a width of 500 ns was generated for each excitation. Although the actual signal deviates slightly from the ideal due to the characteristics of the firing circuit and the PZT element, it still maintains a wide bandwidth. On the receiving side, a 65 dB gain and a wide-bandwidth filter were applied to the received signal. However, due to signal attenuation within the battery and the resonance of the PZT elements, the received signal is narrow-bandwidth, centered at 200 kHz. The sampling frequency was set to 25 MHz, which is sufficient to capture minimal travel time shifts as small as 0.04 μs.

Data collection for the in-plane transducers was performed in full-matrix capture (FMC) mode, where each emitter is sequentially excited while all receivers are active after each excitation. The interval between two excitations was set to more than 1 ms to prevent interference. For the through-thickness PZT transducers, the pitch-catch mode was employed, meaning the waves generated by one transducer were collected only by its directly opposite counterpart. The total time required for each data collection was less than 1 second.

For each diagnosis, data collection was repeated 16 times consecutively to allow for further signal averaging. The total time required for this process was less than 10 seconds, during which the temperature could be considered constant. Diagnoses were performed at 1-minute intervals.

Throughout the investigation of fast discharging, the battery equipped with ultrasonic transducers and connected to the battery tester was put in a climatic test chamber from DERWAS[2], which controls the ambient temperature. The battery tester used for charging/discharging the battery and recording the voltage and current was from Digatron firing circuits (Model: MCT 200-06-6 ME S).

[1] https://www.peakndt.com/products/micropulse-ltpa/
[2] http://www.wxderwas.com/

Signal processing

The collected data for each diagnosis can be represented by a matrix $D \in \mathbb{R}^{m\times n}$, where m represents the number of channels, and n denotes the number of sampling points in the time domain.

Next, the singular value decomposition (SVD) [49] was applied to the data matrix D to eliminate the electromagnetic interference. The rationale is that electromagnetic interference typically exhibits a distinct pattern and lower energy compared to ultrasonic signals. Consequently, both electromagnetic interference and ultrasonic signals can be represented as linear combinations of different linearly independent components, with the interference components having lower energy. The interference can be effectively removed by setting the smaller singular values, which represent the energy of the interference, to zero. Mathematically, this process is described by:

$$D = USV^{\mathrm{T}}, \tag{5}$$

where $U \in \mathbb{R}^{m\times m}$ and $V \in \mathbb{R}^{n\times n}$ are unitary matrices with rows consisting of linearly independent eigenvectors of DD^{T} and $D^{\mathrm{T}}D$ (where T represents the transpose), and $S \in \mathbb{R}^{m\times n}$ is a rectangular diagonal matrix containing non-negative singular values.

To remove the electromagnetic interference, the largest 50 singular values were preserved, while the rest were set to zero, resulting in a modified matrix S_0. The denoised data matrix $\hat{D}$ was then reconstructed as:

$$\hat{D} = US_0V^{\mathrm{T}}. \tag{6}$$

Following SVD denoising, a fast Fourier transform (FFT) was applied for each time-domain signal to further reduce high-frequency noise. Both SVD and FFT denoising were implemented using NumPy in Python.

With the denoised data, the change in travel time $\mathbf{\Delta t}$ is determined using the Pearson correlation coefficient (PCC). The shift in signals that maximizes the PCC between the current data and baseline measurements is identified as $\mathbf{\Delta t}$.

In practice, since temperature changes slowly, resulting in continuous travel time changes, the extraction of $\mathbf{\Delta t}$ will refer to the value extracted during the previous diagnosis (one minute prior). This approach limits the search range to a small, localized area near the previous value, thereby avoiding cycle-skipping under low signal-to-noise ratio (SNR) conditions. Notably, channels with very low SNR were classified as dead channels to prevent their negative impact on the results.

Tomographic reconstruction

For limited-angle tomography, iterative reconstruction methods are preferred over filtered back projection (FBP) [42]. In this study, we use the simultaneous iterative reconstruction technique (SIRT), which is well-suited for limited-angle problems and offers robustness against noise [42, 50]. At the k-th iteration, the reconstruction update is given by [51]

$$\mathbf{\Delta s}^{(k)} = \mathbf{\Delta s}^{(k-1)} - CW^{\mathrm{T}}R\left(W\mathbf{\Delta s}^{(k-1)} - \mathbf{\Delta t}\right), \tag{7}$$

where C and R are diagonal matrices with elements $C[j,j] = 1/\sum_i W[i,j]$ and $R[i,i] = 1/\sum_j W[i,j]$. This update integrates corrections from all channels, providing better noise artifact suppression compared to the basic algebraic reconstruction technique (ART).

The limited-angle problem introduces ill-posedness into the reconstruction process due to insufficient data. To address this, additional prior knowledge should be incorporated as a regularization term [52]. Given the continuous nature of the temperature distribution and its small gradients, we employed the smoothing regularization (Tikhonov regularization) [53–55]. This was achieved using a Gaussian filter from SciPy in Python. A 2-D Gaussian kernel G was used for convolution on the reconstructed slowness map, represented by

$$G[i,j] = \frac{e^{-0.5\left(i^2+j^2\right)}}{\sum_{a=-4}^{4}\sum_{b=-4}^{4} G[a,b]}, \tag{8}$$

where $i \in [-4,4]$ and $j \in [-4,4]$. The slowness map was first reshaped from a 1-D vector $\Delta\mathbf{s} \in \mathbb{R}^{240\times 1}$ to a 2-D matrix $\Delta S \in \mathbb{R}^{16\times 15}$ before the convolution operation and then reshaped back to a 1-D vector after the operation.

The regularization and reconstruction processes are alternated [56, 57], where each iteration of Eq. 7 is followed by a smoothing operation. Initialization is either zero or the previous tomography result $\Delta\mathbf{s}_0$, as the temperature distribution changes continuously over time. The iteration process concludes when the fitting error ϵ no longer decreases or the maximum number of iterations, set at 100, is reached. The entire algorithm is summarized in Algorithm 1.

Algorithm 1 Iterative tomographic reconstruction with smoothing regularization

---

Require: $\Delta\mathbf{t}$ and W
Ensure: $\Delta\mathbf{t} = W\Delta\mathbf{s}$
$\Delta\mathbf{s}^{(0)} \leftarrow \mathbf{0}$ or $\Delta\mathbf{s}_0$
$k \leftarrow 1$
$\epsilon_0 \leftarrow \|W\Delta\mathbf{s}^{(0)} - \Delta\mathbf{t}\|_2$
while $k \leq 100$ **do**
    $\Delta\mathbf{s}^{(k)} \leftarrow \Delta\mathbf{s}^{(k-1)} - CW^{\mathrm{T}}R\left(W\Delta\mathbf{s}^{(k-1)} - \Delta\mathbf{t}\right)$
    $\epsilon \leftarrow \|W\Delta\mathbf{s}^{(k)} - \Delta\mathbf{t}\|_2$
    if $\epsilon \geq \epsilon_0$ **then**
        break
    end if
    $\epsilon_0 \leftarrow \epsilon$
    $\Delta\mathbf{s}^{(k)} \rightarrow \Delta S^{(k)}$
    $\Delta S^{(k)}[m,n] \leftarrow \sum_{i=-4}^{4}\sum_{j=-4}^{4} \Delta S^{(k)}[m+i,n+j]G[i,j]$
    $\Delta S^{(k)} \rightarrow \Delta\mathbf{s}^{(k)}$
    $k \leftarrow k+1$
end while
    return $\Delta\mathbf{s}^{(k)}$

Algorithm 1 was initially demonstrated using synthetic travel time data generated from Eq. 1, based on an arbitrary velocity map designed to mimic real conditions. Random noise following a Gaussian distribution with a standard deviation of 0.17 μs, comparable to the noise level observed in experiments, was added to the synthetic travel times.

The velocity map, depicted in Fig. 8, features a low-velocity region with a maximum difference of 200 m/s, following a Gaussian distribution. This was designed to simulate a local high-temperature region caused by fast charging or discharging.

As illustrated in Fig. 8, the proposed algorithm (SIRT + Smoothing) successfully reconstructs a velocity map that closely resembles the true map. As a reference, the back-projection (BP) method, the most basic reconstruction approach, produces an inaccurate result, likely due to the limited projection angles and noise. Thus, the proposed algorithm demonstrates its effectiveness in overcoming the limited angle challenge and noise.

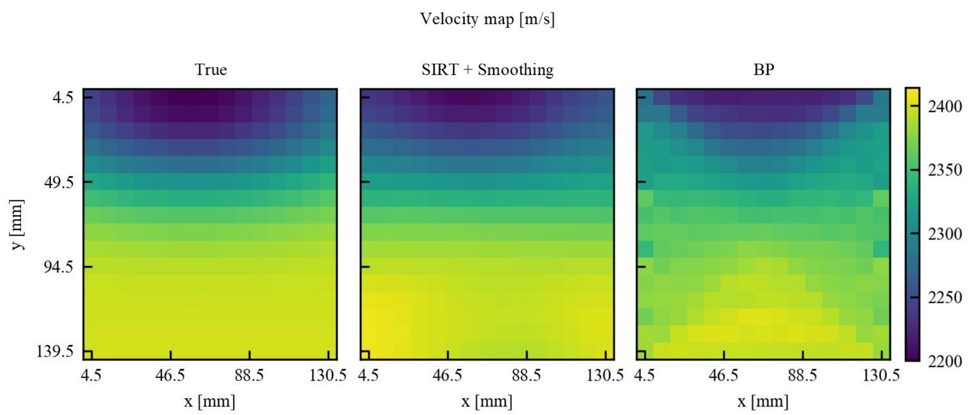

Fig. 8 The true and reconstructed velocity maps using different algorithms.

Acoustic simulation method

The internal structure of the prismatic cell consists of stacked layers. Among these layers, the current collectors (made of Cu and Al) are simple linear elastic solids. The separator, however, is a fluid-saturated porous material, with its solid phase consisting of polypropylene (PP) and a fluid phase of electrolyte. Both the anode and cathode are also porous, with their solid phase comprising several materials listed in Tab. 1, along with an electrolyte fluid phase.

Table 1 Material weight fraction of the prismatic cell.

	Material	Weight
Cathode solid phase	$LiFePO_4$	30.1%
	PVDF	0.8%
	Carbon black	1.3%
Anode solid phase	Graphite	16.5%
	CMC	0.4%
	SBR	0.4%
	Carbon black	0.2%
	Al	17.5%
	Cu	9.7%
	PP	1.9%
	Electrolyte	21.3%

Source: https://www.evebattery.com/
Source: https://www.mtixtl.com/

The complexity of simulating wave propagation in batteries and the effect of temperature on travel time arises primarily from the multi-layer structure and the porous microstructures of the electrode and separator layers.

The electrodes consist of multiple solid materials, making an analytical solution based on Biot theory [58], which assumes a homogeneous solid phase, impractical for this case. To accurately model sound speed across these porous layers, a 3-D numerical model that accounts for micro-scale fluid-solid interactions is necessary [59]. To model wave transmission in both the through-thickness and in-plane directions of the cell, it is crucial to account for the multi-layered structure. In the in-plane direction, wave velocity is influenced by the coupling between different layers, while in the through-thickness direction, multi-reflections at interfaces impact wave velocity [60]. Given the need for such a large-scale model, the finite-difference time-domain (FDTD) method is ideal due to its computational efficiency compared to other numerical methods.

For modeling wave propagation in both fluid and solid media, a velocity-stress formulation can be adopted in FDTD, which describes dynamics in both media. This formulation implicitly handles the fluid-solid interaction between different materials [61]. Material changes and heterogeneities are handled using parameter maps defined for each grid point, eliminating the need for explicitly stated boundary conditions. The formulation in Cartesian coordinates is expressed as follows:

$$\rho(\mathbf{x})\frac{\partial v_i}{\partial t}(\mathbf{x},t) = \sum_{j=1}^{d}\frac{\partial T_{ij}}{\partial x_j}(\mathbf{x},t) + f_i(\mathbf{x},t) \tag{9}$$

and

$$\frac{\partial T_{ij}}{\partial t}(\mathbf{x},t) = \sum_{j=1}^{d}\sum_{i=1}^{d} C_{ijkl}(\mathbf{x})\frac{\partial v_k}{\partial x_l}(\mathbf{x},t) + \theta_{ij}(\mathbf{x},t), \tag{10}$$

where d is the space dimension. $\mathbf{x}$ and t are the space and time variables. $\rho(\mathbf{x})$ is the mass density and $C_{ijkl}(\mathbf{x})$ is the fourth-order stiffness tensor. The components of the particle velocity field are represented by $v_i(\mathbf{x},t)$, and the components of the stress tensor are $T_{ij}(\mathbf{x},t)$. The force sources are denoted by f_i, while θ_{ij} represents the tensor components of strain rate sources. This formulation based on the stiffness tensor allows equally taking into account solid media and fluid media.

The model must be 3-D since, in porous media, both fluids and solids are interconnected, requiring $d = 3$. To solve for the unknown quantities $v_i(\mathbf{x},t)$ and $T_{ij}(\mathbf{x},t)$, the material properties $\rho(\mathbf{x})$ and $C_{ijkl}(\mathbf{x})$ must be specified. For isotropic materials, $C_{ijkl}(\mathbf{x})$ can be described using two independent parameters, bulk modulus K and shear modulus μ.

For the prismatic cell at the fully discharged state and room temperature, the material properties referenced from the literature are listed in Tab. 2. The binder/-carbon composite is treated as a single material at the micro-scale, referred to as conductive binder, as the carbon exists in the form of nanoparticles. The elastic properties of the conductive binder are estimated based on the measured elastic modulus reported in the literature [62, 63] and an assumed Poisson's ratio of 0.35. This value was selected because typical plastics have a Poisson's ratio of around 0.4, while carbon black exhibits a Poisson's ratio of approximately 0.3.

Table 2 Composition mechanical properties of the prismatic cell

Composition	ρ [kg/m^3]	K [GPa]	μ [GPa]
$LiFePO_4$ [64]	3500	95	45
Cathode binder [62] (PVDF&Carbon black)	1964	1.78	0.59
Graphite [65]	2260	27	12.5
Anode binder [63] (CMC&SBR&Carbon black)	1636	0.56	0.19
PP	900	1.38	0.92
Electrolyte [66]	1270	2.49	

The model geometry was constructed in an approximate manner due to the limitations of the FDTD method, which operates on a regular spatial grid and offers limited geometric flexibility.

Considering the material weight fractions listed in Tab. 1, the densities provided in Tab. 2, the cell geometry, and the number of layers revealed by X-ray CT, a spatial step size of 2 μm was chosen to effectively model the microstructures. The active particles ($LiFePO_4$ and graphite) were modeled as cubes with a side length of 16 μm, while the binders were represented as cuboids with dimensions of 8 μm $\times$ 8 μm $\times$ 2 μm, connecting the particles. This approach results in geometric parameters that closely approximate the actual structure, as listed in Tab. 3.

Fig. 9 illustrates the geometry of the FDTD model. A representative unit cell was constructed first, which is symmetric with respect to all six surfaces relative to

Table 3 Geometrical parameters in the FDTD model of the prismatic cell.

Layer	Thickness [μm]	Number of layers	Material	Volume fraction
Cathode	74	152	$LiFePO_4$	51.9%
			Binder	9.9%
			Electrolyte	38.2%
Anode	56	160	Graphite	52.6%
			Binder	9.7%
			Electrolyte	37.7%
Separator	16	160	PP	50%
			Electrolyte	50%
Al	60	76		
Cu	8	80		

adjacent units. Consequently, the Cu and Al layers within the unit cell are modeled with half of their actual thickness. The solid phase of the separator, made of PP, is modeled as a regular frame structure. Given that the separator is not bonded to the electrodes, additional thin layers with a unit thickness of 2 μm were introduced between the separator and the electrodes to simulate weak interfaces [67–70]. These thin layers account for the friction forces, ensuring that stresses remain continuous through their thickness. However, due to the potential for sliding, there can be an in-plane displacement discontinuity. To simulate this behavior, the thin layers are assigned the material properties of PP, with the exception of the shear modulus. A very small but non-zero shear modulus, 0.5% of PP's shear modulus, is used in these layers to ensure shear stress continuity while allowing for in-plane displacement discontinuity.

For the simulation of through-thickness transmission, the representative unit and its through-thickness reflection form a repetitive unit, which is then extended in the z-direction. A plane wave source was applied to the top surface of the model in the z-direction, with transmitted waves received on the bottom surface. Due to the symmetry in both geometry and wavefields, symmetric boundary conditions were imposed on the four side surfaces, creating a quasi-1-D model, as illustrated in Fig. 9a. Similarly, an in-plane transmission model was constructed, as shown in Fig. 9b.

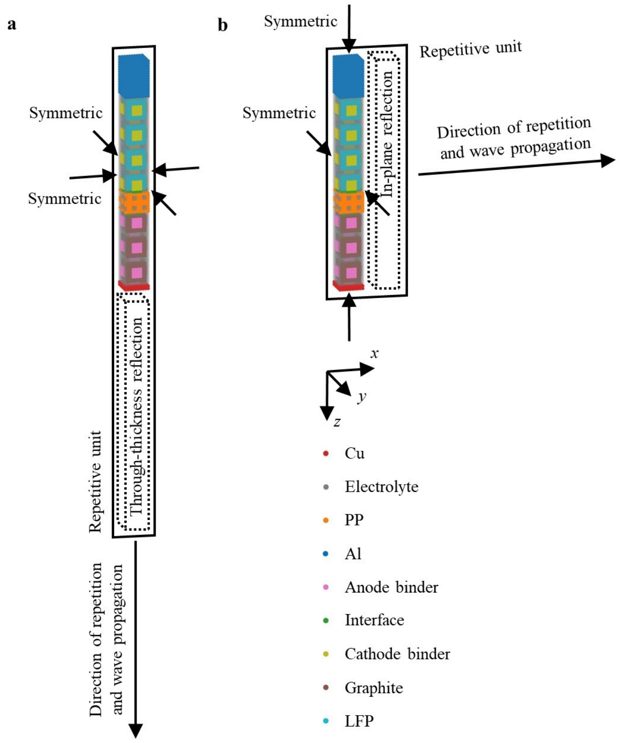

Fig. 9 Acoustic simulation model. a Through-thickness transmission. **b** In-plane transmission.

Given the aforementioned material properties, geometries, and boundary conditions, Equations 9 and 10 were solved using the FDTD method, implemented with the freely available third-party software suite SimSonic [61]. This software employs central-difference approximations for the space and time partial derivatives and discretizes spatial and temporal domains over regular grids defined by a temporal step Δt and a spatial step Δx. Both the time and spatial steps must be sufficiently small to ensure smooth representations of the computed field. The spatial step was inherently small (2 μm) since the micro-scale structures are being modeled. The time step is determined by the Courant-Friedrichs-Lewy (CFL) condition:

$$\Delta t \leq \frac{1}{\sqrt{d}} \frac{\Delta x}{c_{max}}, \tag{11}$$

where c_{max} is the highest sound speed among all sound speeds present in the simulation medium.

Data availability

Data will be provided.

Code availability

The code will be provided.

References

[1] Feng, X. *et al.* Thermal runaway mechanism of lithium ion battery for electric vehicles: A review. *Energy storage materials* **10**, 246–267 (2018).

[2] Drake, S. *et al.* Heat generation rate measurement in a li-ion cell at large c-rates through temperature and heat flux measurements. *Journal of Power Sources* **285**, 266–273 (2015).

[3] Fu, Y. *et al.* An experimental study on burning behaviors of 18650 lithium ion batteries using a cone calorimeter. *Journal of Power Sources* **273**, 216–222 (2015).

[4] Mei, W. *et al.* Operando monitoring of thermal runaway in commercial lithium-ion cells via advanced lab-on-fiber technologies. *Nature communications* **14**, 5251 (2023).

[5] Guo, Z. & Chen, Z. High-temperature capacity fading mechanism for lifepo4/graphite soft-packed cell without fe dissolution. *Journal of Electroanalytical Chemistry* **754**, 148–153 (2015).

[6] Feinauer, M., Wohlfahrt-Mehrens, M., Hölzle, M. & Waldmann, T. Temperature-driven path dependence in li-ion battery cyclic aging. *Journal of Power Sources* **594**, 233948 (2024).

[7] Hosseinzadeh, E. *et al.* A systematic approach for electrochemical-thermal modelling of a large format lithium-ion battery for electric vehicle application. *Journal of power sources* **382**, 77–94 (2018).

[8] Luo, M. *et al.* Fast self-preheating system and energy conversion model for lithium-ion batteries under low-temperature conditions. *Journal of Power Sources* **565**, 232897 (2023).

[9] Liu, J., Zhang, Y., Bai, J., Zhou, L. & Wang, Z. Influence of lithium plating on lithium-ion battery aging at high temperature. *Electrochimica Acta* **454**, 142362 (2023).

[10] Zhao, L. *et al.* Numerical modeling of thermal runaway for low temperature cycling lithium-ion batteries. *Journal of Energy Storage* **63**, 107053 (2023).

[11] Nikolov, N. I., Chahbaz, A., Hildenbrand, F., Kateri, M. & Sauer, D. U. Statistical investigation of temperature-dependent cycle lifetime and cell-to-cell variance in lithium-ion batteries: A model-based approach. *Journal of Power Sources* 235334 (2024).

[12] Ma, S. *et al.* Temperature effect and thermal impact in lithium-ion batteries: A review. *Progress in Natural Science: Materials International* **28**, 653–666 (2018).

[13] Lu, J., Lyu, Y., Chen, B. & Wu, C. Accurate measurement of the internal temperature of 280 ah lithium-ion batteries by means of pre-buried thermocouples. *Batteries* **10**, 184 (2024).

[14] Li, Z. *et al.* Examining temporal and spatial variations of internal temperature in large-format laminated battery with embedded thermocouples. *Journal of Power Sources* **241**, 536–553 (2013).

[15] Wu, B., Li, Z. & Zhang, J. Thermal design for the pouch-type large-format lithium-ion batteries: I. thermo-electrical modeling and origins of temperature non-uniformity. *Journal of The Electrochemical Society* **162**, A181 (2014).

[16] Ghalkhani, M., Bahiraei, F., Nazri, G.-A. & Saif, M. Electrochemical–thermal model of pouch-type lithium-ion batteries. *Electrochimica Acta* **247**, 569–587 (2017).

[17] Mastali, M. *et al.* Electrochemical-thermal modeling and experimental validation of commercial graphite/lifepo4 pouch lithium-ion batteries. *International Journal of Thermal Sciences* **129**, 218–230 (2018).

[18] Xie, Y. *et al.* A novel electro-thermal coupled model of lithium-ion pouch battery covering heat generation distribution and tab thermal behaviours. *International Journal of Energy Research* **44**, 11725–11741 (2020).

[19] He, C., Yue, Q., Wu, M., Chen, Q. & Zhao, T. A 3d electrochemical-thermal coupled model for electrochemical and thermal analysis of pouch-type lithium-ion batteries. *International Journal of Heat and Mass Transfer* **181**, 121855 (2021).

[20] Gao, X. *et al.* Probing inhomogeneity of electrical-thermal distribution on electrode during fast charging for lithium-ion batteries. *Applied Energy* **336**, 120868 (2023).

[21] Li, S., Zhang, C., Zhao, Y., Offer, G. J. & Marinescu, M. Effect of thermal gradients on inhomogeneous degradation in lithium-ion batteries. *Communications Engineering* **2**, 74 (2023).

[22] Zheng, Y. *et al.* Thermal state monitoring of lithium-ion batteries: Progress, challenges, and opportunities. *Progress in Energy and Combustion Science* **100**, 101120 (2024).

[23] Maleki, H. & Howard, J. N. Internal short circuit in li-ion cells. *Journal of Power Sources* **191**, 568–574 (2009).

[24] Ren, Y., Zhang, H., Wei, L., Feng, X. & Wu, W. Multi-layer internal short-circuit mechanism and thermal runaway risk assessment of lithium-ion batteries using nail penetration simulation. *Journal of Energy Storage* **97**, 112824 (2024).

[25] Jia, Y., Zhao, P., Finegan, D. P. & Xu, J. Dynamics of intra-cell thermal front propagation in lithium-ion battery safety issues. *Advanced Energy Materials* 2400621 (2024).

[26] Heenan, T. *et al.* Mapping internal temperatures during high-rate battery applications. *Nature* **617**, 507–512 (2023).

[27] Zhu, S. *et al.* A novel embedded method for in-situ measuring internal multi-point temperatures of lithium ion batteries. *Journal of power sources* **456**, 227981 (2020).

[28] Kisseler, N. *et al.* Monitoring of thermal runaway in commercial prismatic high-energy lithium-ion battery cells via internal temperature sensing. *Batteries* **10**, 41 (2024).

[29] Zhang, Q. *et al.* In situ and real-time monitoring the chemical and thermal evolution of lithium-ion batteries with single-crystalline ni-rich layered oxide cathode. *Angewandte Chemie* **136**, e202401716 (2024).

[30] Peng, J. *et al.* Enhancing lithium-ion battery monitoring: A critical review of diverse sensing approaches. *eTransportation* 100360 (2024).

[31] Vignesh, S. *et al.* State of health (soh) estimation methods for second life lithium-ion battery—review and challenges. *Applied Energy* **369**, 123542 (2024).

[32] Williams, D., Copley, R., Bugryniec, P., Dwyer-Joyce, R. & Brown, S. A review of ultrasonic monitoring: Assessing current approaches to li-ion battery monitoring and their relevance to thermal runaway. *Journal of Power Sources* **590**, 233777 (2024).

[33] Zhang, R. *et al.* State of charge and temperature joint estimation based on ultrasonic reflection waves for lithium-ion battery applications. *Batteries* **9**, 335 (2023).

[34] Owen, R. E. *et al.* Operando ultrasonic monitoring of the internal temperature of lithium-ion batteries for the detection and prevention of thermal runaway. *Journal of The Electrochemical Society* **171**, 040525 (2024).

[35] Duric, N. *et al.* Detection of breast cancer with ultrasound tomography: First results with the computed ultrasound risk evaluation (cure) prototype. *Medical physics* **34**, 773–785 (2007).

[36] Huthwaite, P. & Simonetti, F. High-resolution imaging without iteration: A fast and robust method for breast ultrasound tomography. *The Journal of the Acoustical Society of America* **130**, 1721–1734 (2011).

[37] Holstein, P. *et al.* Acoustic tomography on the basis of travel-time measurement. *Measurement Science and Technology* **15**, 1420 (2004).

[38] Zhu, B. *et al.* A novel reconstruction method for temperature distribution measurement based on ultrasonic tomography. *IEEE Transactions on Ultrasonics, Ferroelectrics, and Frequency Control* **69**, 2352–2370 (2022).

[39] Steinhardt, M. *et al.* Meta-analysis of experimental results for heat capacity and thermal conductivity in lithium-ion batteries: A critical review. *Journal of Power Sources* **522**, 230829 (2022).

[40] Quan, Y. & Huang, L. *Sound-speed tomography using first-arrival transmission ultrasound for a ring array*, Vol. 6513, 48–56 (SPIE, 2007).

[41] Li, C., Duric, N., Littrup, P. & Huang, L. In vivo breast sound-speed imaging with ultrasound tomography. *Ultrasound in medicine & biology* **35**, 1615–1628 (2009).

[42] Kak, A. C. & Slaney, M. *Principles of computerized tomographic imaging* (SIAM, 2001).

[43] Ha, S., Lonkar, K., Mittal, A. & Chang, F.-K. Adhesive layer effects on pzt-induced lamb waves at elevated temperatures. *Structural Health Monitoring* **9**, 247–256 (2010).

[44] Polewczyk, F., Leyssale, J.-M. & Lafourcade, P. Temperature-dependent elasticity of single crystalline graphite. *Computational Materials Science* **220**, 112045 (2023).

[45] Guney, H. Y. Elastic properties and mechanical relaxation behaviors of pvdf (poly (vinylidene fluoride)) at temperatures between- 20 and 100° c and at 2 mhz ultrasonic frequency. *Journal of Polymer Science Part B: Polymer Physics* **43**, 2862–2873 (2005).

[46] Laiarinandrasana, L., Besson, J., Lafarge, M. & Hochstetter, G. Temperature dependent mechanical behaviour of pvdf: Experiments and numerical modelling. *International Journal of Plasticity* **25**, 1301–1324 (2009).

[47] Wang, A. A. *et al.* Compressibility of lithium hexafluorophosphate solutions in two carbonate solvents. *Journal of Chemical & Engineering Data* **68**, 805–812 (2023).

[48] Yu, X. *et al.* Simultaneous operando measurements of the local temperature, state of charge, and strain inside a commercial lithium-ion battery pouch cell. *Journal of The Electrochemical Society* **165**, A1578 (2018).

[49] Rajwade, A., Rangarajan, A. & Banerjee, A. Image denoising using the higher order singular value decomposition. *IEEE Transactions on Pattern Analysis and Machine Intelligence* **35**, 849–862 (2012).

[50] Zhang, Y. *et al.* A comparative study of limited-angle cone-beam reconstruction methods for breast tomosynthesis. *Medical physics* **33**, 3781–3795 (2006).

[51] Van Aarle, W. *et al.* The astra toolbox: A platform for advanced algorithm development in electron tomography. *Ultramicroscopy* **157**, 35–47 (2015).

[52] Rao, J., Ratassepp, M. & Fan, Z. Limited-view ultrasonic guided wave tomography using an adaptive regularization method. *Journal of Applied Physics* **120** (2016).

[53] Virieux, J. & Operto, S. An overview of full-waveform inversion in exploration geophysics. *Geophysics* **74**, WCC1–WCC26 (2009).

[54] Mueller, J. L. & Siltanen, S. *Linear and nonlinear inverse problems with practical applications* (SIAM, 2012).

[55] Huthwaite, P., Zwiebel, A. A. & Simonetti, F. A new regularization technique for limited-view sound-speed imaging. *IEEE transactions on ultrasonics, ferroelectrics, and frequency control* **60**, 603–613 (2013).

[56] Sidky, E. Y., Jørgensen, J. H. & Pan, X. Convex optimization problem prototyping for image reconstruction in computed tomography with the chambolle–pock algorithm. *Physics in Medicine & Biology* **57**, 3065 (2012).

[57] Jones, G. & Huthwaite, P. Limited view x-ray tomography for dimensional measurements. *NDT & E International* **93**, 98–109 (2018).

[58] Carcione, J. M. J. M. *Wave fields in real media: Wave propagation in anisotropic, anelastic, porous and electromagnetic media* (Elsevier, 2007).

[59] Zhang, S., Zuo, P., Yin, X. & Fan, Z. Exploring the correlation between ultrasound time of flight and the state of health of lifepo4 prismatic cells. *Journal of Energy Storage* **83**, 110715 (2024).

[60] Huang, M., Cegla, F. & Lan, B. Stiffness matrix method for modelling wave propagation in arbitrary multilayers. *International Journal of Engineering Science* **190**, 103888 (2023).

[61] Bossy, E. & Grimal, Q. Numerical methods for ultrasonic bone characterization. *Bone quantitative ultrasound* 181–228 (2011).

[62] Grillet, A. M. *et al.* Conductivity degradation of polyvinylidene fluoride composite binder during cycling: Measurements and simulations for lithium-ion batteries. *Journal of The Electrochemical Society* **163**, A1859 (2016).

[63] Hu, H., Tao, B., He, Y. & Zhou, S. Effect of conductive carbon black on mechanical properties of aqueous polymer binders for secondary battery electrode.

Polymers **11**, 1500 (2019).

[64] Maxisch, T. & Ceder, G. Elastic properties of olivine li x fepo 4 from first principles. *Physical Review B* **73**, 174112 (2006).

[65] Qi, Y., Guo, H., Hector, L. G. & Timmons, A. Threefold increase in the young's modulus of graphite negative electrode during lithium intercalation. *Journal of The Electrochemical Society* **157**, A558 (2010).

[66] Gor, G. Y., Cannarella, J., Prévost, J. H. & Arnold, C. B. A model for the behavior of battery separators in compression at different strain/charge rates. *Journal of the Electrochemical Society* **161**, F3065 (2014).

[67] Nagy, P. B. Ultrasonic classification of imperfect interfaces. *Journal of Nondestructive evaluation* **11**, 127–139 (1992).

[68] Baltazar, A., Wang, L., Xie, B. & Rokhlin, S. Inverse ultrasonic determination of imperfect interfaces and bulk properties of a layer between two solids. *The Journal of the Acoustical Society of America* **114**, 1424–1434 (2003).

[69] Lanza di Scalea, F., Rizzo, P. & Marzani, A. Propagation of ultrasonic guided waves in lap-shear adhesive joints: case of incident a 0 lamb wave. *The Journal of the Acoustical Society of America* **115**, 146–156 (2004).

[70] Hosten, B. & Castaings, M. Finite elements methods for modeling the guided waves propagation in structures with weak interfaces. *The Journal of the Acoustical Society of America* **117**, 1108–1113 (2005).

Acknowledgements

Author contributions

Competing interests

The authors declare no competing interests.

Additional information

Supplementary information. A photo of the experimental setup, a video of real-time temperature mapping during external heating, and GIFs illustrating temperature evolution during fast charges/discharges are included as supplementary files.